A 2D Model for Interfacial Recombination in Mesoscopic Perovskite Solar Cells with Printed Back Contact

Lukas Wagner,* Cheng Qiu, Moritz Unmüssig, Dmitry Bogachuk, Simone Mastroianni, Uli Würfel, Yue Hu,* Hongwei Han, and Andreas Hinsch*

A physical model to explain the 2D charge recombination in mesoscopic graphite-based perovskite solar cells (PSCs) having a highly selective front electrode and a nonselective back electrode is presented. Steady-state photovoltage and photoluminescence (PL) as well as transient PL are studied for a wide range of device configurations, providing insights in the interface recombination at the front and back contact, namely, the mesoporous titania (m-TiO$_2$) and the graphite layer. Combining experimental evidence with the first 2D simulation of a perovskite solar cell, it is found that the characteristic thick absorber layer of mesoscopic graphite-based PSC is a necessity to enhance the photovoltage. This is because the interface recombination at the back contact is a diffusion-limited process. The electrode spacing should, however, not be enhanced by increasing the perovskite/m-TiO$_2$ thickness as this increases surface recombination losses at this interface. The study determines design rules for the optimal geometry of the mesoporous layers and helps to identify the limiting recombination pathways for an improvement of future device architectures.

1. Introduction

In only 10 years since the first reports, perovskite solar cells (PSCs) have been improved steadily, reaching certified optical-to-electrical power conversion efficiencies (PCEs) of up to 25.2% (cf. **Figure 1**a). Although these cells still typically have a small active area and often suffer from low stability, their PCEs are among those of well-established photovoltaic (PV) technologies such as silicon PV.[1,2] Due to their unique property of being producible from solution and at low temperatures, e.g., by printing techniques, while at the same time retaining remarkable

defect-tolerant semiconductor properties, perovskites are promising candidates to enter the market as the cheapest PV technology.[3,4] Highest efficiencies are commonly achieved in devices with evaporated metal back electrodes where each layer of the device is deposited one after another, typically by spin coating for laboratory-scale cells.[5–7] In the following, this is referred to as the "metal-based" approach. To become economically competitive, PSC development also needs to meet the criteria of low manufacturing cost and high product lifetimes. Here, high-efficient metal-based PSCs are struggling as the commonly used charge transport hole conductors such as 2,2′,7,7′-Tetrakis[*N*,*N*-di(4-methoxyphenyl)amino]-9,9′-spirobifluorene (spiro-OMeTAD) and gold as metal back electrodes are too expensive for commercialization. Moreover, the organic charge transport layers (CTLs) and metal electrodes induce severe device degradation.[8–10]

As shown in Figure 1b, in contrast to the metal-based approach, the "magic triangle" of efficiency, cost, and lifetime is technologically addressed from the other end by printable mesoscopic PSC with graphite back electrodes, as inspired by dye solar cell research.[11–13] Here, the mesoporous, inorganic CTLs and space layers are printed first to a porous monolith and the perovskite is infiltrated as last processing step.[14,15] As the perovskite decomposes at temperatures above 100–150 °C,[16] only with the mesoscopic graphite-based

L. Wagner, M. Unmüssig, D. Bogachuk, Dr. S. Mastroianni, Dr. U. Würfel, Dr. A. Hinsch
Department Organic and Perovskite Photovoltaics
Fraunhofer Institute for Solar Energy Systems ISE
Heidenhofstraße 2, 79110 Freiburg, Germany
E-mail: andreas.hinsch@ise.fraunhofer.de

The ORCID identification number(s) for the author(s) of this article can be found under https://doi.org/10.1002/solr.202000595.

L. Wagner
Fraunhofer-Gesellschaft zur Förderung der angewandten Forschung e.V.
E-mail: lukas.wagner@ise.fraunhofer.de

C. Qiu, Dr. Y. Hu, Prof. H. Han
Michael Grätzel Center for Mesoscopic Solar Cells
Wuhan National Laboratory for Optoelectronics
Huazhong University of Science and Technology
1037 Luoyu Road, Wuhan 430074, P. R. China
E-mail: yuehu@hust.edu.cn

M. Unmüssig, Dr. S. Mastroianni, Dr. U. Würfel
Freiburg Materials Research Center FMF
University of Freiburg
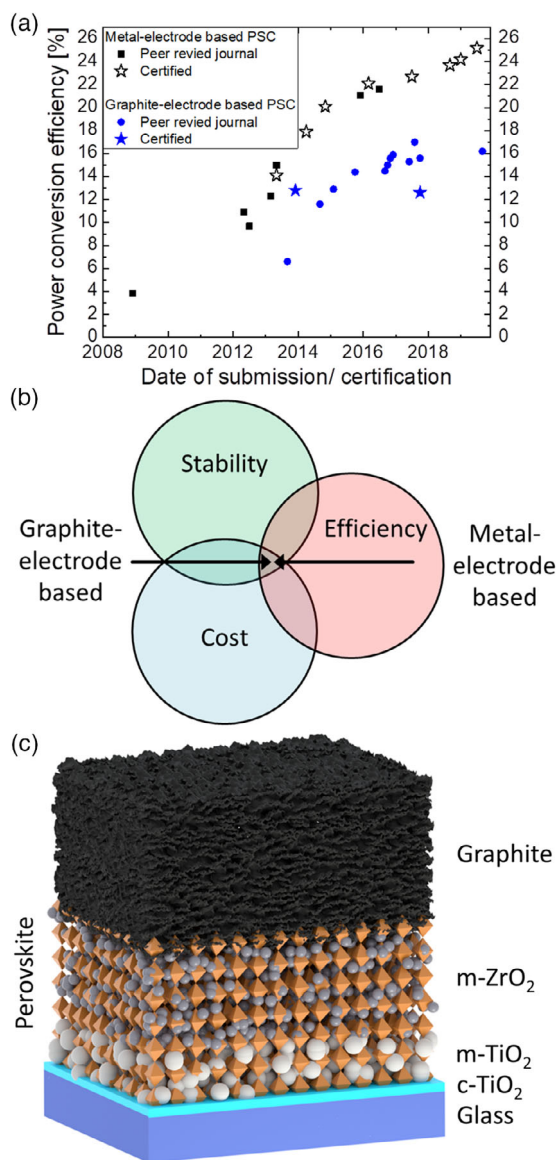Stefan-Meier-Straße 21, 79014 Freiburg, Germany

Figure 1. a) Representative progression of reported and certified power conversion efficiencies of PSCs in the architecture with evaporated metal electrodes and of printed mesoscopic graphite-based devices. b) Schematic illustration of the two concepts' opportunities to approach the economically desirable optimum of high efficiency, long stability, and low cost from opposing sides. c) Layer structure of mesoscopic graphite-based PSC.

the current record architecture in terms of device stability, reaching highest operation lifetimes of up to 10 000 h under 1 sun which corresponds to 10 years of photon flux in central Europe.[17] Likewise, the largest commercial-size perovskite modules have been realized with this printed mesoscopic structure.[3,18] However, device efficiencies are still lacking behind those of metal-based PSC with highest certified values above 12%[15,19] and highest values reported in the literature of exceeding 16%[20–22] (cf. Figure 1a). As high stability and the potential for lowest production costs have been demonstrated by practice and by principle,[23] the next step is thus to explore performance obstacles that currently delay a further increase in the efficiency.

In this work, we investigate the fundamental working principles of mesoscopic graphite-based PSC that lead to a different performance in respect to metal-based devices. We focus on studying the effect of each layer and the respective interfaces, determining dominant charge recombination process and connecting them to open-circuit voltage (V_{oc}) losses. Our study is guided by establishing a novel 2D model for mesoscopic PSC devices with unbalanced charge selectivities. The model is examined experimentally by studying a broad range of mesoscopic graphite-based PSC configurations by steady-state V_{oc} measurements, steady-state photoluminescence (PL), and transient time-resolved PL (TRPL) decay. We further explore the device physics of the model by a complementary 2D drift-diffusion device simulation. We determine three fundamental charge extraction and surface recombination mechanisms: 1) a severe recombination at the graphite back electrode which is mitigated by the beneficial effect of the perovskite layer thickness on the V_{oc} due to diffusion limitation; 2) an improved charge extraction by the mesoporous TiO_2 layer; and 3) a trap-assisted recombination at the TiO_2 surface, which scales with the m-TiO_2 layer thickness. This helps to shine light on the full potential and final limitations of state-of-the-art mesoscopic graphite-based device structures and to construct pathways for further improvements toward highest efficient graphite-based PSC.

2. Theory

Since the first report of efficient mesoscopic graphite-based PSCs by Han's group in 2013,[14,15] much effort has been made to improve the device structure. Yet, until today the general geometry and layer dimensions of the original device have hardly changed. At the same time, the efficiency has not been able to increase at the same pace as for the cells produced by metal-based approach (cf. Figure 1a), with largest improvements achieved by optimizations of the perovskite absorber. A typical mesoscopic PSC stack consists of around 0.4–1 μm of m-TiO_2 and 1–2 μm m-ZrO_2 (cf. **Figure 2**a). In contrast, highest performing metal-based PSCs have absorber layer thicknesses in the range of 500 nm, which is up to 5 times lower. Still, with mesoscopic graphite-based PSC architectures, photovoltages (V_{oc}) beyond 1 V have been reached for methylammonium lead triiodide (MAPbI$_3$) perovskite photoabsorbers.[19] This is 300 mV below the maximum obtainable photovoltage in the radiative limit (V_{oc}^{rad}) for this absorber material.[24] While the best metal-based PSCs already surpassed the mark of 100 mV loss in respect to V_{oc}^{rad},[24] the relatively high photovoltage for mesoscopic

approach it is possible to deposit and sinter chemically highly stable inorganic CTLs and metal-oxide electrodes at elevated temperatures. As shown in Figure 1c, a typical mesoscopic graphite-based PSC stack comprises fluorine-doped tin oxide (FTO) glass for the transparent front contact, coated with a thin, compact hole blocking layer of titanium dioxide (c-TiO_2). The electron extraction is achieved by mesoporous titanium dioxide (m-TiO_2), while holes need to be transported within the perovskite absorber to the back contact made of micronized graphite. TiO_2 and graphite are electrically isolated from each other by a so-called space layer of mesoporous zirconium dioxide (m-ZrO_2). Due to the chemically inert nature of these printed layers, this is
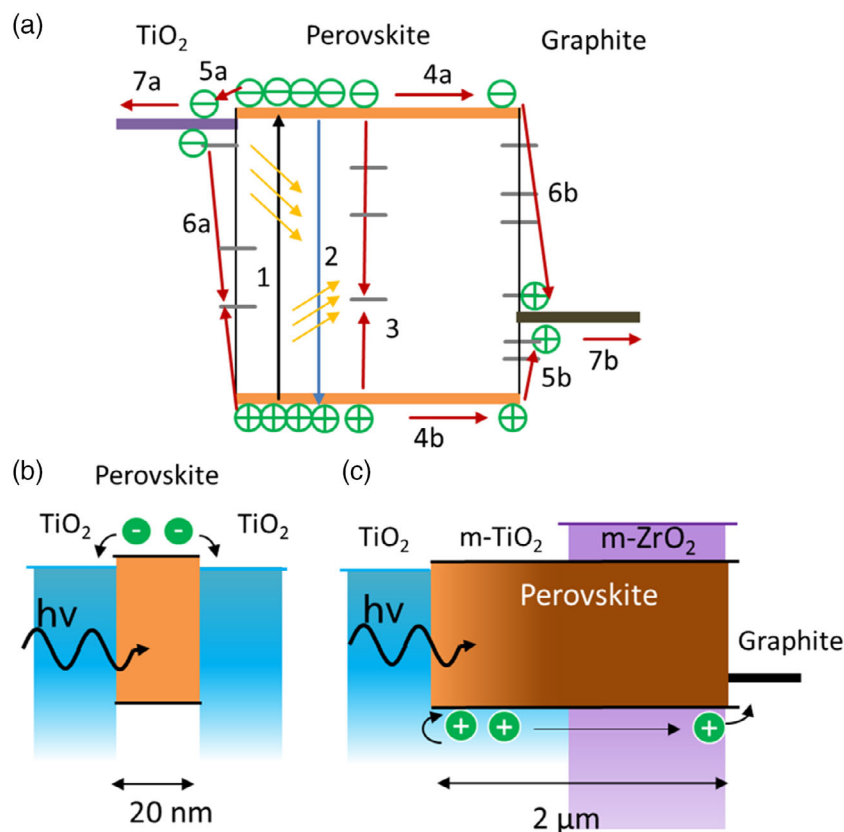
Figure 2. a) Illustration of the fundamental generation, recombination, and transport processes in mesoscopic graphite-based PSC. Depiction of the 2D charge extraction of b) electrons and c) holes at the respective contacts.

graphite-based devices is nevertheless striking considering that the graphite back contact used for hole extraction provides only very poor charge selectivity. The work function of micronized graphite has been determined to range between −4.6,[25] −4.81,[26] and −4.94 eV,[27] which would result in a misalignment with respect to the MAPbI₃ perovskite valence band of at least 0.5 eV. Therefore, graphite-based PSCs have also been referred to as "hole transport layer free" (HTL-free). This is misleading as holes are obviously transported in graphite and thus we do propose the term "hole selective layer free" (HSL-free). Overall, the behavior of HSL-free devices is in stark contrast to the requirement of almost perfectly aligned work functions for metal-based PSCs[28] as, e.g., reported by Huang et al. who predicted that V_{oc} values beyond 900 mV would only be reached for HSLs with work functions above 5.2 eV.[29] In the following, we outline the physical description to explain this seemingly contradictory coexistence of poor band alignment and high photovoltage.

2.1. Fundamental Relations of V_{oc} and Recombination in Solar Cells

Photovoltaic devices work under the fundamental principle of photogeneration and extraction of charge carriers. Under open circuit in steady state, no charges flow out of the device through the outer wirings. Thus, the photovoltage is limited by the recombination processes inside the cell. The recombination mechanisms are of radiative and nonradiative nature. While the first cannot be avoided and should be as high as possible, the latter needs to be minimized. These processes are shown in Figure 2a, showing the mechanisms for photovoltaic power conversion: an electron hole pair is generated by the absorption of a photon in the perovskite (1). In open circuit, it can recombine either radiatively (2) or nonradiatively. Nonradiative recombination can occur directly in the bulk absorber (3) or after injection into the CTLs (5) where they can recombine by surface recombination (6). As charge carriers are generated close to the TiO₂ front electrode, there is a diffusion-assisted charge carrier movement toward the graphite back electrode (4). Finally, if the device is not operated at open circuit, charges can also be extracted by the outer cables (7).

In the limiting case where the external luminescence quantum efficiency approaches the internal one, a simple equation for the V_{oc} can be obtained as[30]

$$V_{oc} = V_{oc}^{rad} + \frac{kT}{q} \ln\left(\frac{R_{rad}}{R_{rad} + R_{nrad}}\right) \qquad (1)$$

where V_{oc}^{rad} is the radiative limit of the open-circuit voltage (1.34 V for MAPbI₃[24]), k is the Boltzmann constant, T is the temperature, and q is the elementary charge. The radiative and nonradiative recombination rate is represented by R_{rad} and R_{nrad}, respectively.

R_{nrad} is reciprocal proportional to the effective lifetime for nonradiative recombination, τ_{eff}^{nrad}, which for perovskites essentially comprises of the bulk (τ_b) and surface (τ_s) recombination lifetimes. Herein, the latter is the limiting factor for most PSC devices because perovskites typically display remarkably high bulk recombination lifetimes[31,32]

$$\tau_{eff}^{nrad-1} = \tau_b^{-1} + \tau_s^{-1} \tag{2}$$

τ_b is the material-specific Shockley–Read–Hall (SRH) recombination lifetime which is essentially dependent on the trap density of the perovskite. The bulk lifetime for the negative (n) and positive (p) charge carriers is related to the respective diffusion length L and diffusion coefficient D.

$$\tau_{b,n} = \frac{L_n^2}{D_n} \tag{3a}$$

$$\tau_{b,p} = \frac{L_p^2}{D_p} \tag{3b}$$

Thus, to reduce the bulk recombination rate, the average transport distance of the respective charge carriers toward "their" contact in the solar cell should be considerably lower than the respective diffusion length.

τ_s, on the other hand, is governed by the recombination at the interface between perovskite and the respective charge extraction layer (CEL) which is strongly dependent on the "selectivity" of the CEL, i.e., the ability to accept one charge carrier and repel the other. Thus, it is commonly concluded that to maximize the V_{oc} of a perovskite device, both the purity of the bulk perovskite material and the selectivity of the CELs and quality of the interface are imperative.

So how can mesoscopic graphite-based devices with poorly selective graphite back contact achieve such high photovoltages? The puzzle can be solved by a closer look at the surface lifetime. While there is no general analytical solution to determine τ_s, Sproul,[33] based on the work of Otaredian,[34] derived a range of useful approximations. If we consider a PV cell with absorber layer thickness d and surface recombination velocities S_1 and S_2 at each CEL interface, the time-dependent o1D diffusion equation for one type of charge carriers yields two approximate solutions: if the surface velocity is equal on both interfaces ($S_1 = S_2 = S$), then

$$\tau_s \approx \frac{d}{2S} + \frac{d^2}{D\pi^2} \tag{4a}$$

The second case is given if one of the surface velocities approaches zero. For $S_2 = 0$, we obtain

$$\tau_s \approx \frac{d}{S_1} + \frac{4d^2}{D\pi^2} \tag{4b}$$

These two cases already suffice to assess the behavior of the surface recombination. They demonstrate that the nonradiative recombination rate which needs to be minimized is proportional to a function depending on $S \times d^{-1}$ and $D \times d^{-2}$. For the case of one highly selective contact (Equation (4b)), this relation tells us that, figuratively, the further away the other, poorly selective

interface is from the selective one, the lower the surface recombination at the "bad" contact. Even for an infinite surface recombination S_1, τ_s will be nonzero due to the second term on the right-hand side of the equations accounting for the diffusion to the contact, which proceeds at a finite time and thus limits the recombination of charges at the surface. Moreover, the fact that most carriers are generated close to the front contact also helps to minimize losses at the back contact. Overall, this explains why mesoscopic graphite-based PSC with poor band alignment at the back contact and thus high surface recombination velocities are still able to reach moderately high V_{oc} values by the often-overlooked effect of an increased device thickness.

2.2. The Concept of 2D Charge Extraction in Mesoscopic PSC

These considerations lead to the model of 2D charge extraction in mesoscopic PSC with nonselective back electrodes. The model is based on the postulates that perovskite has an absorption coefficient to essentially absorb all light within the first 0.5–1 μm of perovskite embedded in a porous structure[35–37] and that the diffusion length of holes is larger than this absorption depth.[31] For the model, we suppose two hypotheses that we will examine in the following:

Hypothese 1 (TiO$_2$):
H1.1: For the advantage of mesoscopic scale, TiO$_2$ is strongly charge selective and effectively extracts photogenerated electrons from the perovskite.

H1.2: At the same time, TiO$_2$ induces a nonzero surface recombination. Thus V_{oc} decreases with higher m-TiO$_2$ thickness.

Hypothese 2 (electrode spacing):
A wider spacing between the electrodes, i.e., a thicker perovskite layer implemented by a thicker m-ZrO$_2$ space layer, increases the V_{oc} due to reduced surface recombination at the graphite interface, as expressed in Equation (4b).

With this, we can derive the following model for mesoscopic graphite-based PSC, as shown in Figure 2b. In these devices, the perovskite absorber is embedded in nanopores composed of mesoscopic nanoparticles (20 nm) of m-TiO$_2$ or m-ZrO$_2$. Photogenerated electrons in the m-TiO$_2$ region are efficiently extracted into the TiO$_2$ with an average transport distance within the absorber below 10 nm. As this is order of magnitudes lower than the electron diffusion length and with TiO$_2$ being a very selective electron extraction material (EEM), this leads to low bulk and surface recombination rates for the electrons. If electrons are generated inside the m-ZrO$_2$ region, the mean free path is much longer, but not necessarily larger than L_n. The density of electrons generated inside the perovskite-filled pores of the m-ZrO$_2$ essentially depends on the thickness of the m-TiO$_2$ layer and with it on how far the absorption profile reaches into the bulk of the cell.

For the photogenerated holes, the situation looks very differently (cf. Figure 2c). They need to migrate all the way to the back electrode throughout the porous structures, which results in an average charge transport in the order of the electrode spacing d (i.e., the thickness of both m-TiO$_2$ and m-ZrO$_2$). As shown in Figure 2b,c, this extends the typically 1D continuity representation to a 2D problem with different transport directions for elections and holes. Once the holes reach the graphite interface, due

to the poor band alignment, there is a high probability for surface recombination with electrons. From Equation (3) and (4), we find that as long as $d < L_{n,p}$, to reduce surface recombination it is beneficial to increase d. In the following section, we present and discuss evidence for the validity of this perception.

3. Results and Discussion

3.1. Effect of the Electrode Spacing on V_{oc}

To study the effect of electrode spacing, the m-ZrO$_2$ thickness was varied while the m-TiO$_2$ layer thickness was kept constant at 350 nm. **Figure 3**a shows the progression of the steady-state V_{oc} with the m-ZrO$_2$ thickness, measured under a class A solar simulator. Looking at the scattered data points, it is most significant to regard the highest V_{oc} values for each configuration as this gives an indication of the maximal possible photovoltage. Lower values can be attributed to imperfections during processing, e.g., during printing, pore filling, and crystallization. Considering the highest values, one can observe a clear trend of increasing V_{oc} with higher m-ZrO$_2$ layer thickness. Starting at photovoltages below 0.81 V for m-ZrO$_2$ thicknesses of 0.5 μm, the V_{oc} increases steeply to 0.91 V at 2.2 μm. Here, the curve saturates, reaching a highest value of 0.93 V for 3.7 μm of m-ZrO$_2$. We remark that with increasing layer thickness, the filling of the pores becomes less controllable (cf. Section 1.1, Supporting Information), which might explain the lower

values for devices with 3.0 and 4.4 μm m-ZrO$_2$. It is noted that at very low m-ZrO$_2$ layer thicknesses below 1 μm, the probability of spot-wise direct electrical connections between TiO$_2$ and graphite due to variations during screen-printing increases which could further lower V_{oc} (experimental evidence is provided in the in Section 1.2, Supporting Information).

3.2. Effect of m-TiO$_2$ Thickness on V_{oc}

Figure 3c shows the steady-state V_{oc} for samples with different m-TiO$_2$ thickness at a constant m-ZrO$_2$ thickness of 2.2 μm. The samples shown in plots (a) and (c) were fabricated at Huazhong University of Science and Technology (HUST), yielding reverse-scan PCEs of up to 12%. The I–V characteristics are shown in the Supporting Information. Overlapping samples with 350 nm m-TiO$_2$ and 2.2 μm m-ZrO$_2$ thickness are marked in empty boxes in both Figure 3a,c. There is a rise in V_{oc} between thicknesses of 120 nm of m-TiO$_2$ to 560 nm from up to 0.88 V to up to 0.93 V. After these thicknesses, the photovoltage again decreases to below 0.57 V for 6 μm. Notably, for samples without m-TiO$_2$ ("0 nm", compact TiO$_2$ only), the highest V_{oc} is even as low as 0.41 V.

The progression of V_{oc} indicates that we observe a superposition of two independent effects influencing charge carrier recombination: first, a decrease in V_{oc} with increasing m-TiO$_2$ thickness becomes dominant for an m-TiO$_2$ thickness beyond 1 μm. Although m-TiO$_2$ is highly charge selective, the surface
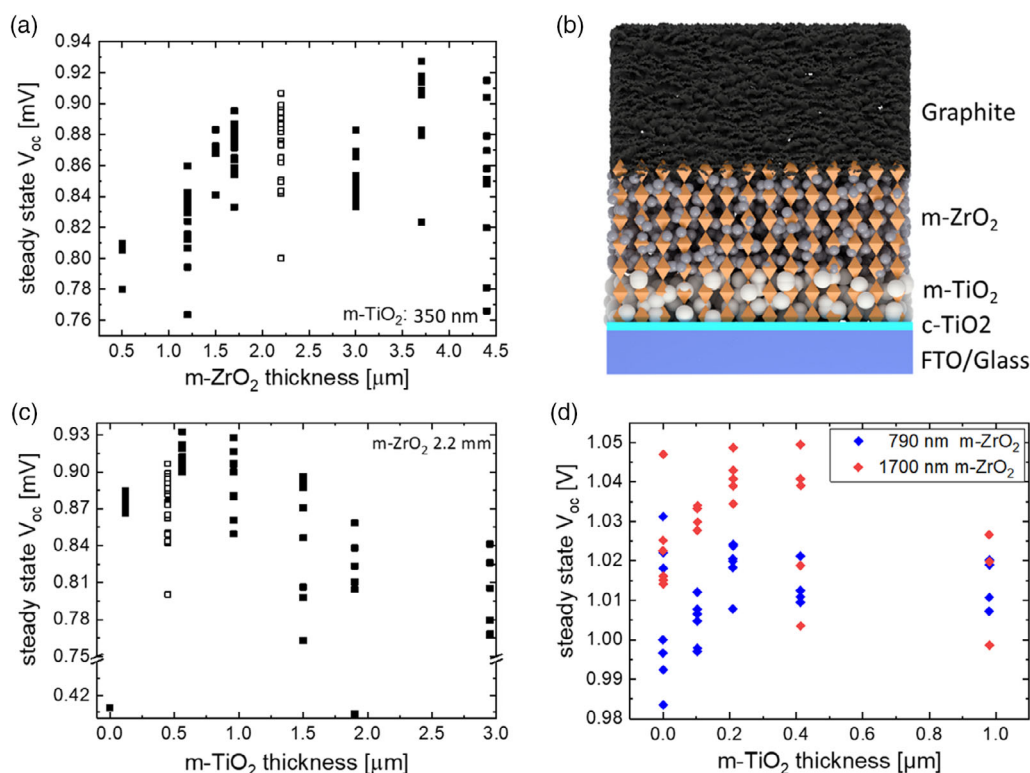

Figure 3. Steady-state V_{oc} values for a variation of the a) m-ZrO$_2$ and c,d) m-TiO$_2$. The layer structure is sketched in part (b). The devices of (a,c) have been fabricated at HUST with 10–20 devices for each variation. The empty-box data-points refer to identical samples in each plot. Devices of (d) were fabricated at ISE with seven samples per variation for devices with 0.79 (blue) and 1.7 μm (red) thick m-ZrO$_2$ layers. Measurements were carried out under simulated AM1.5G light.

recombination at this interface is nonzero. In accordance with the study of Lee et al.,[38] we thus observe that with increasing m-TiO$_2$/perovskite interface area, surface recombination between electrons in the TiO$_2$ and holes in the perovskite increases, as shown later by PL measurements.

A second effect, which is only observed in this specific set of samples, leads to a decrease in V_{oc} for very thin m-TiO$_2$ layers and a drastic collapse for m-TiO$_2$-free devices. The introduction of only 120 nm mesoporous m-TiO$_2$ leads to a significant increase in the V_{oc} in contrast to the m-TiO$_2$-free device. Inside the nanoporous m-TiO$_2$ network, the mean free path for photogenerated electrons to reach the CTL is decreased drastically to below 10 nm. Simultaneously, the larger interface area leads to a more efficient charge extraction; a rough estimate (assessing m-TiO$_2$ by simple packing of spherical TiO$_2$ particles of 10 nm radius) yields that the TiO$_2$/perovskite interface increases over 60-fold with respect to the pure compact layer for every 100 nm of m-TiO$_2$. A possible explanation for the decreasing photovoltage would be that in the studied devices the c-TiO$_2$ or more likely voids in the c-TiO$_2$ layer exposing the FTO layer induce a higher surface recombination. This could partially be mitigated if electrons are injected into the m-TiO$_2$ instead. Finally, it is also possible that the perovskite crystal quality is altered in the different structures, thus influencing the photovoltage. These considerations are examined by PL studies in the following section.

Another batch of samples with the same perovskite composition was fabricated at Fraunhofer ISE to examine the aforementioned presumptions that the observed effect of decreasing V_{oc} is caused by specific technological constraints and not due to universally valid fundamental recombination mechanisms. The same commercially available m-TiO$_2$ printing paste as used for the samples fabricated by HUST was used and the c-TiO$_2$ layer was also deposited by manual spray pyrolysis. Figure 3d shows the obtained steady-state V_{oc} values for ISE samples with 0.79 (blue) and 1.7 μm (red) thick m-ZrO$_2$ layers over a range of m-TiO$_2$ thicknesses. Here, the highest PCE was significantly lower with highest reverse-scan PCEs of 7%. However, remarkably high stabilized photovoltages of up to 1.05 V were reached. It is noted that in all experiments, for thin m-TiO$_2$ layers the J_{sc} (and respectively the PCE) was very low. Revealingly, in the samples of Figure 3d, the V_{oc} did not decrease as severely for smaller m-TiO$_2$ thicknesses; for single samples there was even an increase in photovoltage for the m-TiO$_2$-free device. Overall, this indicates that the trend shown in Figure 3c is probably due to artifacts from the device processing. The trend of decreasing photovoltage for thicker m-TiO$_2$ layers is, however, still present.

Overall, we conclude that the V_{oc} trend toward higher m-TiO$_2$ layer thicknesses can be attributed to a universally valid effect, most likely recombination at the m-TiO$_2$/perovskite interface, whereas no general statements can be made for the V_{oc} trend toward low m-TiO$_2$ thicknesses.

3.3. Charge Extraction and Surface Recombination at the Interfaces

To elucidate our conjectures further, steady-state and transient PL measurements were carried out on the samples processed

at HUST. **Figure 4**a,b shows the steady-state PL intensity of respective devices for different m-ZrO$_2$ and m-TiO$_2$ thickness. The PL intensity qualitatively follows the trend of the V_{oc}. This indicates that the difference in V_{oc} for different thicknesses is mainly due to differences in the quasi-Fermi-level splitting (QFLS) (compare also Section 2.1, Supporting Information).[39,40]

Figure 4c,d shows the complementary TRPL measurements of the samples. For the following section, it is important to keep in mind that due to the fast repetition of the excitation pulse of this typical TRPL setup, it is probable that the probed system is not in steady state at the time when the decay is induced. As outlined in Figure 2a, under open-circuit conditions, the reduction of the population of photogenerated charge carriers and thus PL decay is determined by the superposition of four processes: there are two recombination processes in the bulk, namely, radiative and nonradiative bulk recombination. At the interfaces, if the system is not in steady state ("transient") there are two processes of charge extraction to the CTLs (leading to charge separation and suppression of PL) and interface recombination. If the system is in steady state, only the latter determines the recombination rate at the interface. If the processes would be independent of each other, this would result in a four-exponential decay function. However, the processes are nonlinear and changing carrier concentrations cause an interdependence of the processes.[41] If nevertheless the PL decay is to be assessed by exponential fits, simulations suggest that, for the transient case, the fastest process be attributed to charge extraction, followed by interface recombination.[41,42] Connecting the fastest decay times to interface effects is in agreement with a vast range of experimental results, showing a significantly higher PL lifetime for bulk perovskite in contrast to perovskite in contact to a CTL.[31,43] Although this representation needs to be taken with caution, we fit the TRPL measurements with a biexponential decay function and determined two lifetimes τ_1 and τ_2. In contrast to the steady-state PL measurements, we observe no significant changes of the lifetimes over a wide variation of the m-ZrO$_2$ thickness (Figure 4c). This indicates that although in the steady-state case the PL is reduced by recombination especially at the graphite electrode, the interface recombination at the graphite and ZrO$_2$ interface as well as the bulk recombination are not the fastest processes.

Investigating the TRPL lifetimes for different m-TiO$_2$ thicknesses (Figure 4d) completes this picture: here, a clear decrease in both lifetimes can be observed, indicating that recombination at the perovskite/TiO$_2$ interface is the fastest process. The steady-state PL rises for m-TiO$_2$ thicknesses up to 500 nm, which is in agreement with the reduced influence of the nonradiative recombination induced by c-TiO$_2$ interface. On the contrary, both lifetimes decrease already starting from 120 nm-thick m-TiO$_2$ which promotes that charge extraction (τ_1) and interface recombination (τ_2) are the fastest processes at the m-TiO$_2$ interface. Significantly, the decrease in τ_1 saturates at approximately 1 μm of m-TiO$_2$, decreasing from 7.5 to approximately 4 ns. Note that the thickness to reach saturation is the same range where the thickness exceeds the range of light absorption and photogeneration. On the contrary, τ_2 keeps steadily decreasing throughout the range of layer thicknesses from 75 to below 10 ns. As shown later by numerical simulations, this indicates further that τ_1 is related to (beneficial) charge extraction of photogenerated electrons into the TiO$_2$, a process that is mainly
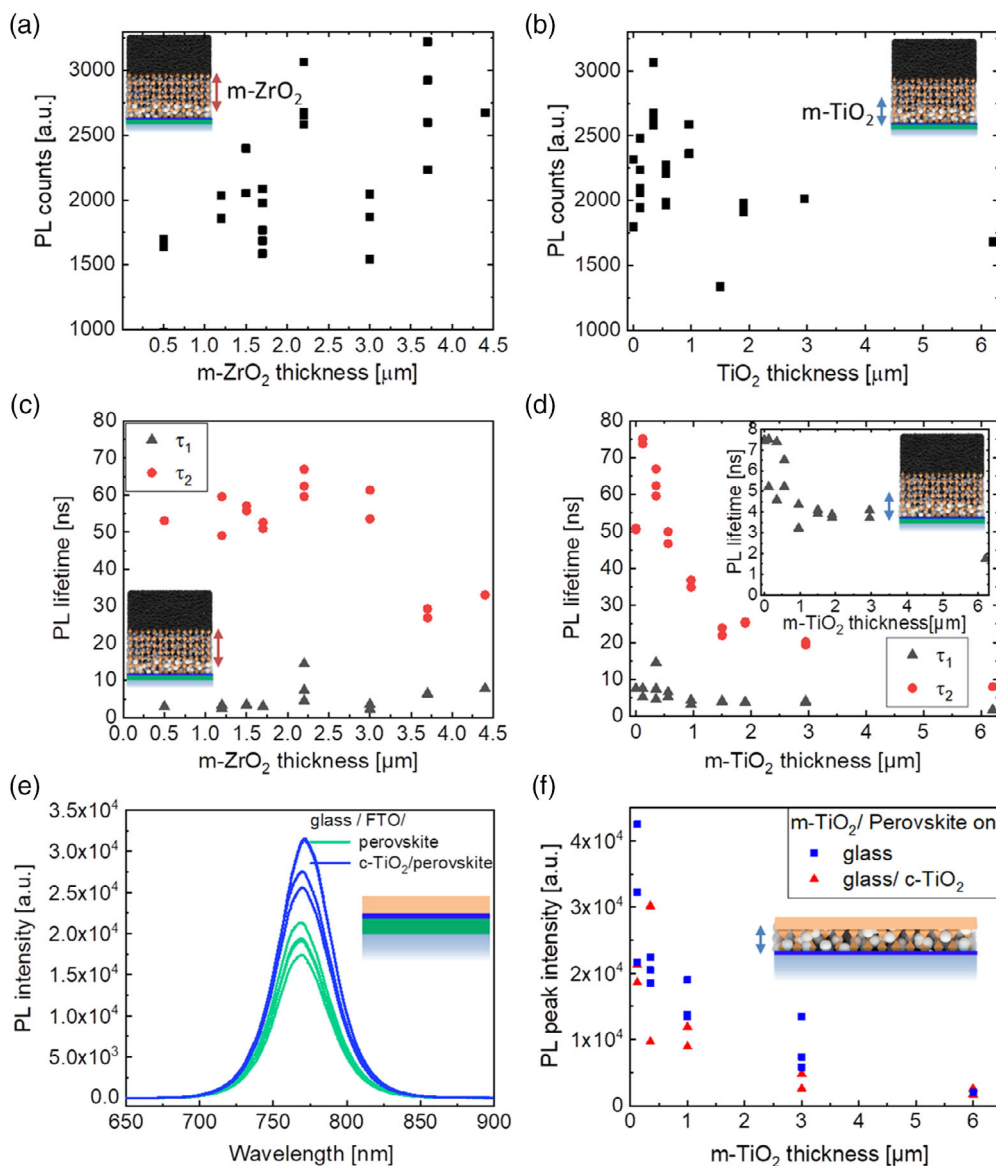
Figure 4. PL investigations of the effect of porous layer thickness for devices made at HUST. Steady-state PL intensity of full devices for a variation of the a) m-ZrO$_2$ and b) m-TiO$_2$ thickness. c,d) Corresponding TRPL lifetimes extracted from a biexponential fit. e) Steady-state PL spectra of samples with perovskite spin cast on FTO glass with and without c-TiO$_2$. Steady-state PL intensity for samples without m-ZrO$_2$ and graphite back electrode for m-TiO$_2$ deposited on bare glass and on glass/c-TiO$_2$. Note that the units of the PL intensities in (a,b) have been recorded on a different setup than for (e,f) and are therefore not comparable.

occurring within the illuminated region of the m-TiO$_2$. As the electrons are extracted into the m-TiO$_2$, they can also distribute toward the "dark" regions. Thus, the probability for interface recombination with holes in the perovskite ($\approx 1/\tau_2$) increases with higher m-TiO$_2$ thickness.

3.4. The Role of the Compact TiO$_2$ Blocking Layer and FTO

The compact c-TiO$_2$ hole blocking layer is crucial to prevent charge recombination at the FTO front electrode. This is evident from Figure 4e and Figure S6, Supporting Information, showing that the steady-state PL and TRPL lifetime, respectively, increase

with the addition of a c-TiO$_2$ layer in comparison to perovskite being in direct contact with FTO.

Coming back to Figure 4d, a closer look at the devices without m-TiO$_2$ ("0 nm") in comparison to devices with 120 nm of m-TiO$_2$ shows that, while the value of τ_1 remains the same, there is a steep increase in τ_2 from 50 to 75 ns accompanied by an increase in the V_{oc}. This can be interpreted to the effect that the velocity of charge extraction from the perovskite to the TiO$_2$ is the same for the compact and mesoporous case, but the surface recombination at these interfaces is strongly reduced by adding the m-TiO$_2$ layer. This conception is further supported by the observation that the PL lifetimes (τ_1, τ_2) for the m-TiO$_2$ free devices are independent from

the m-ZrO$_2$ thickness over a wide range between 0.5 and 4 µm (cf. Figure S7, Supporting Information).

The picture is completed by an investigation of the differences between the compact and mesoporous TiO$_2$ layer, eliminating the effect of the m-ZrO$_2$ layer and graphite back electrode, as compared by steady-state PL measurements in Figure 4f. Here, m-TiO$_2$ was screen printed on substrates of bare glass (blue) and glass/c-TiO$_2$ (red) and infiltrated with perovskite. One can see that, in accordance to the results shown earlier (cf. Figure 4b), an increasing m-TiO$_2$ thickness has a strong influence on reducing the PL intensity. Revealingly, there is a reduction of PL intensity for all layer thicknesses when c-TiO$_2$ is used as under-layer, suggesting that c-TiO$_2$ has an even higher contribution to surface recombination.

3.5. Diffusion Limitation Can Mitigate Reduced QFLS

To further test our hypotheses, we conducted numerical simulations with the commercial semiconductor device simulation tool Sentaurus TCAD from Synopsys Inc. for a Beer–Lambert-like generation profile (i.e., no optics were considered). To accurately reproduce the experimental results, a 2D device model had to be implemented, this way properly mimicking the mesoporous layers. As shown in **Figure 5**a, the porosity of the m-TiO$_2$ and perovskite was modeled by two separate laminar structures placed next to each in a direction perpendicular to the cell thickness resembling a "pore diameter" of 20 nm, as proposed by Ferber and Luther for DSC.[44] To the best of our knowledge, this is the first study based on a 2D model of mesoscopic perovskite solar cells. The poor selectivity of the hole contact was simulated by a work function that reaches 0.4 eV from the valence band into the perovskite bandgap in combination with a high surface recombination velocity. As the mesoporous ZrO$_2$ serves merely as a geometrical spacer, we have regarded ZrO$_2$ as an inert electrical insulator. The effective semiconductor layer where the perovskite is infiltrated into the m-ZrO$_2$ is represented by the band energies of a pure perovskite layer. Efficient charge extraction into the m-TiO$_2$ and c-TiO$_2$ layers is implemented aligning the conduction band minimum of the TiO$_2$ with the one of the perovskites at −4.0 eV. In the calculation, SRH recombination accounted to less than 1 mV of photovoltage. Consequently, to keep the parameter space of model as small as possible, inside the bulk perovskite layer we considered only direct recombination and also no mobile ions. Further simulation details are listed in the Supporting Information.

The photovoltages resulting from the simulations are shown in Figure 5b. To replicate the experimental data of the HUST samples (Figure 3a,c), trap-assisted recombination at the m-TiO$_2$ interface had to be assumed while, first, no traps at the c-TiO$_2$ interface were implemented (filled symbols). Thereby, both the increase in V_{oc} for increasing m-ZrO$_2$ thicknesses and the decrease in V_{oc} for higher m-TiO$_2$ thicknesses can be reproduced accurately.

To emulate for the drastic decrease in V_{oc} for very thin m-TiO$_2$ layers that was experimentally observed for the samples made at HUST, it was necessary to implement additional recombination at the c-TiO$_2$ layer in the simulation. In the case "with c-TiO$_2$ recombination" (empty symbols), the trap density for hole traps

at the c-TiO$_2$ interface was increased drastically by a factor of 5.6×10^5 with respect to the m-TiO$_2$ trap density. The effect could not be reproduced in the simulation by surface SRH recombination or electron traps. Note that in the experimental device, a similar effect could also be due to recombination between perovskite and FTO, induced by incomplete covering of FTO with c-TiO$_2$. In this case, the model can replicate the entire progression of the data points from Figure 3c; however, the V_{oc} is underestimated by an offset of approximately 50 mV.

To study the effect of electrode spacing, in the following we focus on the dataset without additional recombination at the c-TiO$_2$ interface. Figure 5c,d shows the simulated energy diagrams under illumination at open-circuit conditions of devices with 0.2 and 2.2 µm of m-ZrO$_2$, yielding a QFLS of 0.85 and 0.91 eV, respectively, as marked by the green lines. The higher QFLS in the thicker device is accompanied by a less pronounced upbending of the perovskite valence and conduction band as well as hole QFL toward the hole contact side on the right. This can be explained by Equation (4a) and (4b) which predict that the surface recombination lifetime at the back electrode is proportional to d^2/D. Therefore, an increased electrode spacing d delays the diffusion of both charge carriers to the graphite contact. This effect is enhanced due to the exponential, Beer–Lambert-type generation profile, as photogeneration of charge carriers happens predominately close to the FTO front contact. To outline this effect further, in the Supporting Information we plotted the extreme case of homogeneous generation throughout the entire perovskite layer. Even here, the effect of diffusion limitation dominates.

Although it is beyond the scope of this work, it is noted that the layer thickness does not only influence the photovoltage. As shown in the Supporting Information, especially the m-TiO$_2$ thickness has a strong impact on the short circuit current density due to increased surface recombination. The increased electrode spacing enhances to charge transport losses and thereby reduces the fill factor.

3.6. Junction Formation at the FTO and m-TiO$_2$ Contact

On the side of the electron contact (toward the left of the plots in Figure 5), the band energies are strongly influenced by the FTO layer underneath the 20 nm thin c-TiO$_2$. In correspondence to experimental reports,[45,46] in our model the FTO work function is 0.5 eV beneath the conduction band of the perovskite and the FTO is treated as a metal. As the materials of the FTO/c-TiO$_2$/perovskite heterojunction possess different work functions, as expressed in Poisson's equation, this leads to charge redistribution until the potentials are in equilibrium which, in turn, is reflected by a steep upbending of the perovskite valence and conduction bands at the FTO contact. The corresponding high positive electric field at this interface is shown in Figure 5e,f.

This is already a remarkable finding as in most energy band representations of PSCs, a TiO$_2$ electron contact without FTO is considered. In such a scenario, the conduction and valence band of the perovskite bend down at the TiO$_2$ contact. However, a closer look at the TiO$_2$/perovskite interface within the m-TiO$_2$ layer, i.e., within the modeled nanoparticles, is revealing. If
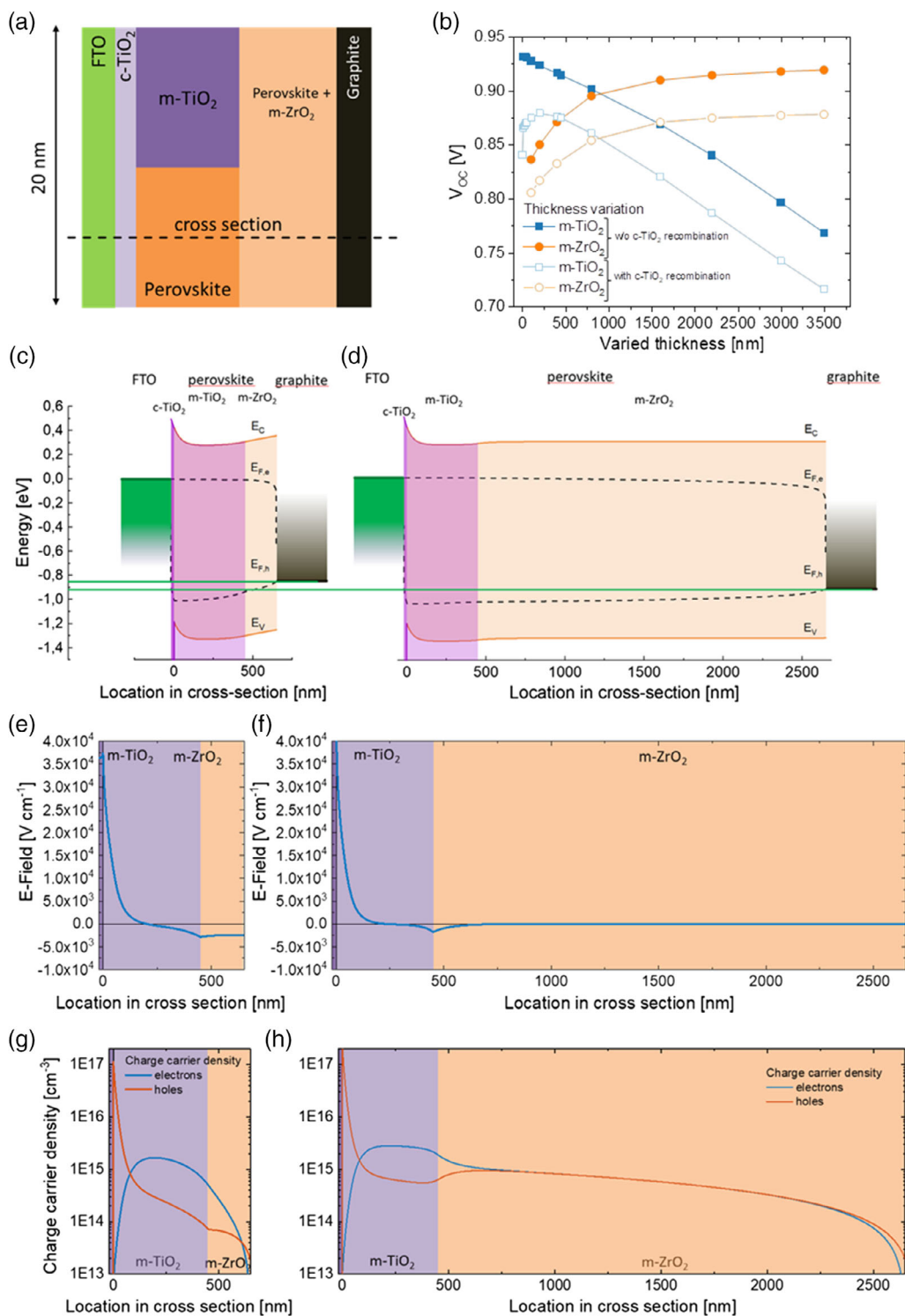
Figure 5. Results of the 2D simulation. a) Illustration of a cross section through the modeled unit cell of the 2D simulation, representing the porous structures inside the device. The dashed line marks the cross section for the following figures, whereas the origin is set to the FTO/c-TiO$_2$ interface. b) Calculated V_{oc} for different layer thicknesses. Band energies along the cross section for a device with both 0.45 μm m-TiO$_2$ and an m-ZrO$_2$ thickness of c) 0.2 and d) 2.2 μm in V_{oc} under illumination. The QFLS is marked by horizontal green lines. e,f) Corresponding electric field and g,h) densities of free charge carriers for the respective device configurations. c–h) Correspond to the case without additional recombination at the c-TiO$_2$ layer.

we consider a profile perpendicular to the cross-section axis considered in Figure 5 in the m-TiO$_2$ region (i.e., a cross section through a nanoparticle), between the 20 nm-thick perovskite and 20 nm-thick TiO$_2$ layer there is no significant difference

in the conduction band minimum and electron density due to the small dimensions. As a consequence, in Figure 5c,d, the conduction band minimum of the m-TiO$_2$ (purple) follows precisely the conduction band minimum of the perovskite (orange). This finding is in accordance with the predictions in the early works of Albery and Bartlett for small colloidal particles.[47] For the valence band, however, there is an energetic barrier at the junction between perovskite and TiO$_2$ such that holes are blocked from entering the TiO$_2$ particles, as shown in Figure S12, Supporting Information.

At the FTO side, the progression of the energy bands is mainly defined by the physical properties of the perovskite and FTO, whereas the influence of the very thin c-TiO$_2$ is negligible. Therefore, the conduction band at the FTO/c-TiO$_2$/perovskite interface resembles a typical metal/semiconductor junction, which is accompanied by a depletion of free electrons (cf. Figure 5g,h). However, as mentioned earlier, holes are effectively blocked to enter the thin c-TiO$_2$. In turn, no typical Schottky junction is formed but there is a strong accumulation of holes in the perovskite at the c-TiO$_2$ interface.

The high, positive electric field at the TCO interface and small negative electrical field at the transition between the perovskite inside the m-TiO$_2$ and the perovskite inside the m-ZrO$_2$ is in good agreement with electric field distribution estimated experimentally by a kelvin probe force microscopy (KPFM) study reported by Bergmann et al. for devices with HSL[48] and is comparable to the results of the KPFM study by Jiang et al. who used a different baseline for the measurement.[49] The presence of an electric field at the TiO$_2$/perovskite junction has also been experimentally predicted in devices with a HSL (spiro-OMeTAD) based on Mott–Schottky analysis[50] and electron beam-induced current (EBIC).[51] For HSL-free devices with a gold back electrode only (TiO$_2$/perovskite/Au), similar studies were also performed by Mott–Schottky analysis[52,53] and EBIC.[51] In accordance with our simulations, they revealed an electric field at the TiO$_2$ but none at the back-electrode interface with the perovskite.

The accumulation of free holes reduces drastically within the first 80 nm of the m-TiO$_2$ layer while the electron concentration increases. Throughout most of the rest of the m-TiO$_2$ region the concentration of free electrons is at least 3 times higher than the concentration of free holes for the displayed two cases.

In the perovskite conduction band, the increasing density of free electrons inside the m-TiO$_2$ region is reflected by a slight downbending. However, it has to be considered that for the charge carrier density, only free carriers are displayed whereas the trapped ones are not shown. The electrical field is considerably low in the m-TiO$_2$ region beyond the FTO contact and is even changing signs from positive to negative (e.g., at 230 nm for the thick device; Figure 5f).

As can be seen from the thick device, in the m-ZrO$_2$ region the conduction and valence band are flat, the electric fields are very low, and there is no significant difference between electron and hole concentration (cf. Figure 5d,f,h). At the graphite interface, a low negative electric field (100 V cm^{-1}) builds up which is due to the difference in electron and hole concentration at the graphite interface.

Concluding, we can compare our new findings with the early considerations by Etgar's group on the working mechanisms of

HSL-free PSC.[52,53] They reported a depletion region at the TiO$_2$/perovskite interface which was interpreted as n/p junction and concluded that the perovskite acts both as a light harvester and a hole conductor. Our findings do not contradict to this picture but show that, considering the 2D mesoscopic nature of the devices, the situation is more complex. Especially, it is not necessary to assume a p-doping of the perovskite in the m-ZrO$_2$ region to explain the presence of an electric field at the m-TiO$_2$/m-ZrO$_2$ junction. Moreover, in our simulation we were able to assume the same carrier mobilities for both holes and electrons. Yet, due to the decoupled, 2D charge extraction, effectively only the transport of the holes to the back contact is limiting in perspective of charge extraction.

3.7. Recombination Currents

Finally, the simulation results can also be used to examine the predictions made earlier based on PL measurements. **Figure 6**a shows the current densities of electrons (yellow) and holes (blue) from the perovskite flowing toward the m-TiO$_2$ interface. The currents were calculated directly at the interface. To illustrate the effect of recombination at the TiO$_2$ interface, a configuration with a very thick (1.6 μm) m-TiO$_2$ layer was chosen. In addition, the optical generation of charge carriers is plotted in red. This shows that the photogenerated electrons and holes move differently toward the TiO$_2$ interface: while the electrons move more directly toward the TiO$_2$, the holes distribute more evenly. At this point it is important to remember that the device is under V_{oc} in steady state. This means that no charges are flowing out of the cell, i.e., throughout the entire device every electron current is related to a recombination with an equivalent hole current. The exact location of the interface recombination is signified by the hole current density toward the interface. The overlap between the electron and hole current curves represents the charge carriers that directly recombine when reaching the m-TiO$_2$ interface from the perovskite side. However, a considerably higher number of holes than electrons only move to the TiO$_2$ interface outside the range of significant generation (in the "dark"). This can be explained by the concept shown in Figure 6b: the electrons that have entered the m-TiO$_2$ in the illuminated region distribute inside the highly electron-conductive m-TiO$_2$ layer into the nonilluminated region. This increases the probability of trap-assisted recombination of holes at the m-TiO$_2$/absorber interface outside the region of photogeneration. In other words, this means that thicker m-TiO$_2$ layers increase the TiO$_2$/perovskite surface area, thereby initially improving the charge extraction and thus the V_{oc} and fill factor. For thicker m-TiO$_2$ layers, however, the beneficial effect of electron injection becomes negligible and is overcompensated by parasitic trap recombination that reduces the V_{oc}. Our experimental data suggest that the ideal m-TiO$_2$ thickness for this optimization problem lies in the region of the optical generation depth.

The dominant recombination mechanism for different device stacks is illustrated by the bar diagram in Figure 6c. In addition, the squares indicate the simulated V_{oc} (right axis). Revealingly, the recombination at the graphite interface is not necessarily the dominant loss mechanism. Revealingly, for the reference structure (0.45/2.2) that yielded high photovoltages in the experiments
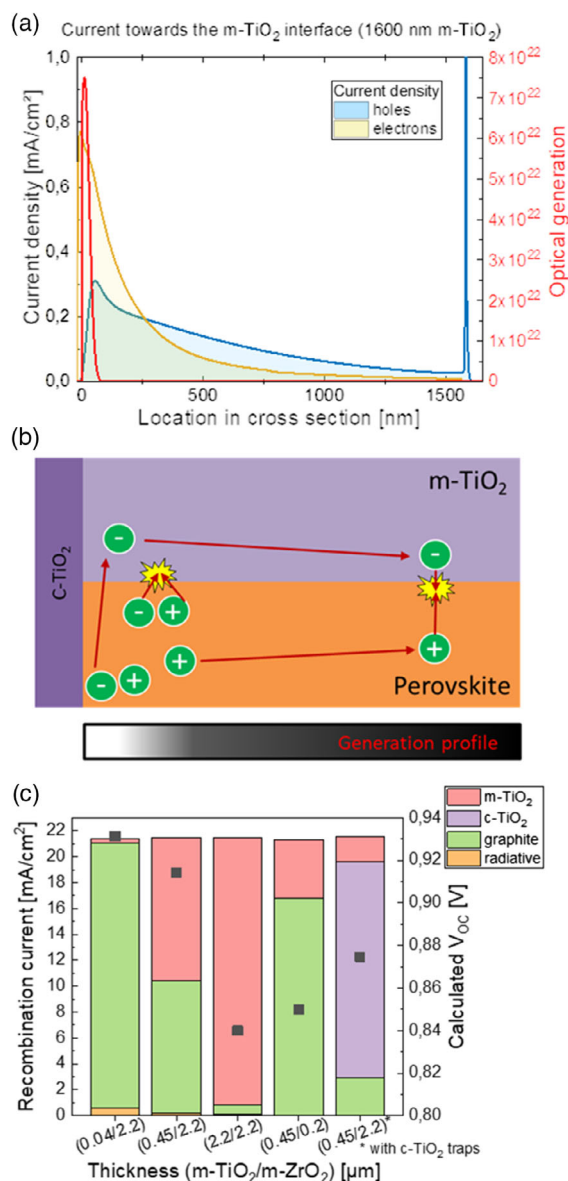
Figure 6. Recombination currents toward the interfaces. a) Calculated current densities of electrons (yellow) and holes (blue) from the perovskite to the m-TiO$_2$ interface as well as the generation profile (red) for a for a very thick m-TiO$_2$ layer of 1.6 μm. b) Correspondingly, a schematic representation of the flow of charge carriers. Contribution of the different recombination mechanisms for a range of layer thicknesses. c) Calculated recombination currents (left axis) for different stacks (indicated by thicknesses of m-TiO$_2$/m-ZrO$_2$). For the bar on the right, also recombination at the c-TiO$_2$ is considered. The squares indicate the achieved V_{oc} (right axis).

and simulations, the graphite and m-TiO$_2$ interface account in even parts for the relevant recombination losses. As outlined earlier, recombination at the m-TiO$_2$ interface dominates if this layer is very thick. In turn, recombination at the graphite electrode prevails if the electrode spacing is reduced by a thin m-ZrO$_2$ layer (0.45/0.2). Moreover, for very thin m-TiO$_2$ (0.04/2.2), graphite recombination can be dominating at high photovoltages. However, if surface recombination at the c-TiO$_2$

(or respective FTO) is considered, this accounts for the highest recombination losses if m-TiO$_2$ is too thin. It is noted that ideally the sum of the recombination currents should be identical for all devices; the small differences are attributed to artifacts from the calculation.

4. Conclusion

We performed a comprehensive study of the impact of different layers on charge carrier recombination in graphite-based, hole selective layer-free mesoscopic PSC. Combining experimental data with a novel 2D simulation of the mesoporous devices, it was found that, if the back electrode is poorly selective as in the case of graphite, an effective way to improve the V_{oc} is an increase in the electrode spacing by the m-ZrO$_2$ space layer thickness. This extends the diffusion path length for charge carriers to reach the back electrode, thus mitigating the surface recombination rate at the back electrode. This effect of beneficial diffusion limitation is restricted to m-ZrO$_2$ layers of few micrometers both by the diffusion length in the bulk perovskite (mainly reducing the fill factor) and, technologically, by increasing challenges in pore filling. Finally, this study demonstrates that in contrast to previous conceptions, a thick m-ZrO$_2$ layer is not only important as an electrical insulation but it represents also a necessary geometric spacer to reduce surface recombination at the graphite electrode.

As for the electron selective layer, for m-TiO$_2$ thicknesses beyond the light absorption depth of approximately 1 μm, the V_{oc} decreases severely. Here, the high electron conductivity of TiO$_2$ leads to a distribution throughout the m-TiO$_2$ also into the nonilluminated regions where trap-assisted surface recombination with the holes from the perovskite side increases with increasing layer thickness.

Overall, our study underlines the importance to simulate the recombination pathways in mesoscopic PSC by a 2D model to identify the limiting process for a given device structure. To approach the radiative limit of the photovoltage, not only the graphite interface should be considered but in fact, all interfaces of the CELs need to be improved.

5. Experimental Section

Materials: Lead iodide (PbI$_2$) and gamma-butyrolactone (GBL) were purchased from Sigma-Aldrich. Methylammonium iodide (MAI) and 5-ammoniumvaleric acid iodide (5-AVAI) were purchased from MaterWin Technology, China. Dimethyl sulfoxide (DMSO) was purchased from Acros Organics. All the materials were used as received without further purification.

Full Cells Fabrication: FTO-coated glasses were etched with an electrode pattern using a 1064 nm laser, and sequentially cleaned with detergent, deionized water, and ethanol for 20 min. After drying, we sprayed the compact TiO$_2$ precursor solution, comprising 9.7 g titanium di-isopropoxytitanium bis(acetylacetonate) (Sigma-Aldrich) added to 79 g isopropanol, to form compact TiO$_2$ precursor solution at 450 °C on the surface of cleaned FTO substrates to obtain the compact TiO$_2$ (c-TiO$_2$) layer. After cooling to room temperature, the mesoporous TiO$_2$ layer (120 nm, 350 nm, 560 nm, 960 nm, 1.5 μm, 1.9 μm, 2.96 μm, or 6.2 μm) was screen printed on top of the c-TiO$_2$layer, and then sintered at 500 °C for 40 min. Subsequently, the mesoporous ZrO$_2$ layer (500 nm, 1.2 μm, 1.5 μm, 1.7 μm, 2.2 μm, 3 μm, 3.7 μm, or 4.4 μm) and 10 mm carbon layer were screen printed and

sintered at 400 °C for 40 min. After cooling down to room temperature, 4.5 μL $(5\text{-AVA})_{0.035}(MA)_{0.965}PbI_3$ perovskite precursor solution (0.3068 g MAI, 0.0172 g 5-AVAI, and 0.9220 g PbI_2 were dissolved in 2 mL GBL, and then stirred at 60 °C overnight) was dropped and infiltrated into the triple mesoporous layers and annealed at 50 °C for 4 h.

Layer Stack Fabrication ("Half Cells"): Spin-coated films were prepared by antisolvent method. Before the spin-coating process, the substrates were dealt with by UV irradiation to remove any remaining organic residues. $(5\text{-AVA})_{0.035}(MA)_{0.965}PbI_3$ perovskite precursor solution (40 μL) was spin-coated on the substrate at 1000 rpm for 10 s and then 6000 rpm for 25 s, then drop 100 μL of chlorobenzene at 27 s, followed by annealing at 50 °C for 10 min. The printed "Half-cells" were prepared in the same way as the full devices, except that the number of layers was different.

Characterization: Steady-state V_{OC} measurements were recorded with a Keithley 2400 source meter under constant simulated AM1.5g illumination from a class A Xenon arc lamp light source.

Steady-state PL measurements for Figure 4a,b were recorded with an optical PL microscope setup by a sCMOS camera (Andor Zyla 5.5), whereas light below 760 nm was filtered out. The sample was illuminated with a 632 nm light-emitting diode (Thorlabs Solis). The photon flux of the light source was calibrated to correspond to 1 sun by calibration with the spectral response of a silicon reference solar cell.

PL intensity spectra of half cells (Figure 4e,f) were recorded on LabRAM HR800 (Horiba Jobin Yvon) with the excitation wavelength of 532 nm.

TRPL decay transients were measured at PL emission wavelengths above 760 nm with a 478 nm excitation laser from the Horiba Scientific DeltaPro. The lifetime was obtained by fitting the spectra with a biexponential decay function.

Supporting Information

Supporting Information is available from the Wiley Online Library or from the author.

Conflict of Interest

The authors declare no conflict of interest.

Author Contributions

L.W. and C.Q. contributed equally to this work. L.W. together with A.H. and H.H. conceived the idea of unidirectional selective charge extraction and the initial model. L.W. and C.Q., together with A.H., U.W., and Y.H.,

designed the experiments. C.Q. fabricated all samples. C.Q. carried out photoluminescence measurements and analysis. L.W. and D.B. carried out steady-state V_{oc} measurements. M.U., L.W., and U.W. designed the concept of the simulations. M.U. made the simulations. M.U. and L.W. analyzed the simulation results. L.W. wrote the manuscript and constructed the illustrations. All authors contributed throughout the project with valuable discussions and reviewed the manuscript. This work emerged from a research visit of L.W. at HUST. The hospitality is gratefully acknowledged by L.W.

[1] A. Kojima, K. Teshima, Y. Shirai, T. Miyasaka, _J. Am. Chem. Soc._ **2009**, _131_, 6050.

[2] M. A. Green, E. D. Dunlop, J. Hohl-Ebinger, M. Yoshita, N. Kopidakis, A. W. Y. Ho-Baillie, _Prog. Photovoltaics_ **2020**, _28_, 3.

[3] Y. Rong, Y. Hu, A. Mei, H. Tan, M. I. Saidaminov, S. I. Seok, M. D. McGehee, E. H. Sargent, H. Han, _Science_ **2018**, _361_, eaat8235.

[4] H. J. Snaith, _Nat. Mater._ **2018**, _17_, 372.

[5] H.-S. Kim, C.-R. Lee, J.-H. Im, K.-B. Lee, T. Moehl, A. Marchioro, S.-J. Moon, R. Humphry-Baker, J.-H. Yum, J. E. Moser, M. Gratzel, N.-G. Park, _Sci. Rep._ **2012**, _2_, 591.

[6] J. Burschka, N. Pellet, S.-J. Moon, R. Humphry-Baker, P. Gao, M. K. Nazeeruddin, M. Grätzel, _Nature_ **2013**, _499_, 316.

[7] M. M. Lee, J. Teuscher, T. Miyasaka, T. N. Murakami, H. J. Snaith, _Science_ **2012**, _338_, 643.

[8] A. K. Jena, Y. Numata, M. Ikegami, T. Miyasaka, _J. Mater. Chem. A_ **2018**, _6_, 2219.

[9] Y. Kato, L. K. Ono, M. V. Lee, S. Wang, S. R. Raga, Y. Qi, _Adv. Mater. Interfaces_ **2015**, _2_, 1500195.

[10] K. Domanski, J.-P. Correa-Baena, N. Mine, M. K. Nazeeruddin, A. Abate, M. Saliba, W. Tress, A. Hagfeldt, M. Grätzel, _ACS Nano_ **2016**, _10_, 6306.

[11] A. Kay, M. Grätzel, _Euro Sun 2004_ **1996**, _44_, 99.

[12] S. Burnside, S. Winkel, K. Brooks, V. Shklover, M. Grätzel, A. Hinsch, R. Kinderman, C. Bradbury, A. Hagfeldt, H. Pettersson, _J. Mater. Sci.: Mater. Electron._ **2000**, _11_, 355.

[13] H. Han, U. Bach, Y.-B. Cheng, R. A. Caruso, C. MacRae, _Appl. Phys. Lett._ **2009**, _94_, 103102.

[14] Z. Ku, Y. Rong, M. Xu, T. Liu, H. Han, _Sci. Rep._ **2013**, _3_, 3132.

[15] A. Mei, X. Li, L. Liu, Z. Ku, T. Liu, Y. Rong, M. Xu, M. Hu, J. Chen, Y. Yang, M. Gratzel, H. Han, _Science_ **2014**, _345_, 295.

[16] A. Dualeh, N. Tétreault, T. Moehl, P. Gao, M. K. Nazeeruddin, M. Grätzel, _Adv. Funct. Mater._ **2014**, _24_, 3250.

[17] G. Grancini, C. Roldán-Carmona, I. Zimmermann, E. Mosconi, X. Lee, D. Martineau, S. Narbey, F. Oswald, F. de Angelis, M. Grätzel, M. K. Nazeeruddin, _Nat. Commun._ **2017**, _8_, 15684.

[18] Y. Hu, Y. Chu, Q. Wang, Z. Zhang, Y. Ming, A. Mei, Y. Rong, H. Han, _Joule_ **2019**, _3_, 2076.

[19] L. Wagner, S. Chacko, G. Mathiazhagan, S. Mastroianni, A. Hinsch, _ACS Energy Lett._ **2018**, _3_, 1122.

[20] S. Liu, W. Huang, P. Liao, N. Pootrakulchote, H. Li, J. Lu, J. Li, F. Huang, X. Shai, X. Zhao, Y. Shen, Y.-B. Cheng, M. Wang, _J. Mater. Chem. A_ **2017**, _5_, 22952.

[21] H. Zhang, H. Wang, S. T. Williams, D. Xiong, W. Zhang, C.-C. Chueh, W. Chen, A. K.-Y. Jen, *Adv. Mater.* **2017**, *29*, 1606608.

[22] Q. Wang, W. Zhang, Z. Zhang, S. Liu, J. Wu, Y. Guan, A. Mei, Y. Rong, Y. Hu, H. Han, *Adv. Energy Mater.* **2020**, *10*, 1903092.

[23] L. Wagner, S. Mastroianni, A. Hinsch, *Joule* **2020**, *4*, 882.

[24] L. Krückemeier, U. Rau, M. Stolterfoht, T. Kirchartz, *Adv. Energy Mater.* **2019**, *10*, 1902573.

[25] L. Zhang, T. Liu, L. Liu, M. Hu, Y. Yang, A. Mei, H. Han, *J. Mater. Chem. A* **2015**, *3*, 9165.

[26] M. Duan, C. Tian, Y. Hu, A. Mei, Y. Rong, Y. Xiong, M. Xu, Y. Sheng, P. Jiang, X. Hou, X. Zhu, F. Qin, H. Han, *ACS Appl. Mater. Interfaces* **2017**, *9*, 31721.

[27] P. Jiang, Y. Xiong, M. Xu, A. Mei, Y. Sheng, L. Hong, T. W. Jones, G. J. Wilson, S. Xiong, D. Li, Y. Hu, Y. Rong, H. Han, *J. Phys. Chem. C* **2018**, *122*, 16481.

[28] M. Stolterfoht, P. Caprioglio, C. M. Wolff, J. A. Márquez, J. Nordmann, S. Zhang, D. Rothhardt, U. Hörmann, Y. Amir, A. Redinger, L. Kegelmann, F. Zu, S. Albrecht, N. Koch, T. Kirchartz, M. Saliba, T. Unold, D. Neher, *Energy Environ. Sci.* **2019**, *12*, 2778.

[29] Y. Huang, S. Aharon, A. Rolland, L. Pedesseau, O. Durand, L. Etgar, J. Even, *EPJ Photovoltaics* **2017**, *8*, 85501.

[30] T. Kirchartz, L. Krückemeier, E. L. Unger, *APL Mater.* **2018**, *6*, 100702.

[31] S. D. Stranks, G. E. Eperon, G. Grancini, C. Menelaou, M. J. P. Alcocer, T. Leijtens, L. M. Herz, A. Petrozza, H. J. Snaith, *Science* **2013**, *342*, 341.

[32] M. Stolterfoht, C. M. Wolff, J. A. Márquez, S. Zhang, C. J. Hages, D. Rothhardt, S. Albrecht, P. L. Burn, P. Meredith, T. Unold, D. Neher, *Nat. Energy* **2018**, *3*, 847.

[33] A. B. Sproul, *J. Appl. Phys.* **1994**, *76*, 2851.

[34] T. Otaredian, *Solid-State Electron.* **1993**, *36*, 153.

[35] P. Löper, M. Stuckelberger, B. Niesen, J. Werner, M. Filipič, S.-J. Moon, J.-H. Yum, M. Topič, S. de Wolf, C. Ballif, *J. Phys. Chem. Lett.* **2015**, *6*, 66.

[36] J. M. Ball, S. D. Stranks, M. T. Hörantner, S. Hüttner, W. Zhang, E. J. W. Crossland, I. Ramirez, M. Riede, M. B. Johnston, R. H. Friend, H. J. Snaith, *Energy Environ. Sci.* **2015**, *8*, 602.

[37] M. Anaya, G. Lozano, M. E. Calvo, W. Zhang, M. B. Johnston, H. J. Snaith, H. Míguez, *J. Phys. Chem. Lett.* **2015**, *6*, 48.

[38] D. G. Lee, M.-C. Kim, B. J. Kim, D. H. Kim, S. M. Lee, M. Choi, S. Lee, H. S. Jung, *Appl. Surf. Sci.* **2017**, *477*, 131.

[39] Z. Hameiri, A. Mahboubi Soufiani, M. K. Juhl, L. Jiang, F. Huang, Y.-B. Cheng, H. Kampwerth, J. W. Weber, M. A. Green, T. Trupke, *Prog. Photovoltaics* **2015**, *23*, 1697.

[40] W. Tress, N. Marinova, O. Inganäs, M. K. Nazeeruddin, S. M. Zakeeruddin, M. Graetzel, *Adv. Energy Mater.* **2015**, *5*, 1400812.

[41] B. Krogmeier, F. Staub, D. Grabowski, U. Rau, T. Kirchartz, *Sustainable Energy Fuels* **2018**, *2*, 1027.

[42] W. Tress, *Adv. Energy Mater.* **2017**, *131*, 1602358.

[43] Y. Hu, Z. Zhang, A. Mei, Y. Jiang, X. Hou, Q. Wang, K. Du, Y. Rong, Y. Zhou, G. Xu, H. Han, *Adv. Mater.* **2018**, *30*, 1705786.

[44] J. Ferber, J. Luther, *J. Phys. Chem. B* **2001**, *105*, 4895.

[45] S. Ravishankar, S. Gharibzadeh, C. Roldán-Carmona, G. Grancini, Y. Lee, M. Ralaiarisoa, A. M. Asiri, N. Koch, J. Bisquert, M. K. Nazeeruddin, *Joule* **2018**, *2*, 788.

[46] Y. Rong, Y. Hu, S. Ravishankar, H. Liu, X. Hou, Y. Sheng, A. Mei, Q. Wang, D. Li, M. Xu, J. Bisquert, H. Han, *Energy Environ. Sci.* **2017**, *10*, 2383.

[47] W. J. Albery, *J. Electrochem. Soc.* **1984**, *131*, 315.

[48] V. W. Bergmann, S. A. L. Weber, F. Javier Ramos, M. K. Nazeeruddin, M. Grätzel, D. Li, A. L. Domanski, I. Lieberwirth, S. Ahmad, R. Berger, *Nat. Commun.* **2014**, *5*, 5001.

[49] C.-S. Jiang, M. Yang, Y. Zhou, B. To, S. U. Nanayakkara, J. M. Luther, W. Zhou, J. J. Berry, J. van de Lagemaat, N. P. Padture, K. Zhu, M. M. Al-Jassim, *Nat. Commun.* **2015**, *6*, 1.

[50] A. Guerrero, E. J. Juarez-Perez, J. Bisquert, I. Mora-Sero, G. Garcia-Belmonte, *Appl. Phys. Lett.* **2014**, *105*, 133902.

[51] E. Edri, S. Kirmayer, S. Mukhopadhyay, K. Gartsman, G. Hodes, D. Cahen, *Nat. Commun.* **2014**, *5*, 3461.

[52] W. A. Laban, L. Etgar, *Energy Environ. Sci.* **2013**, *6*, 3249.

[53] S. Aharon, S. Gamliel, B. El Cohen, L. Etgar, *Phys. Chem. Chem. Phys.* **2014**, *16*, 10512.

2000595 (13 of 13)